Research Square

Preprints are preliminary reports that have not undergone peer review.
They should not be considered conclusive, used to inform clinical practice,
or referenced by the media as validated information.

Multiparametric CEST MRI–Guided Intranasal Theranostic Liposomes for Quantitative Biodistribution and Response Prediction in Glioblastoma

Kannie W. Y. Chan

KannieW.Y.C@cityu.edu.hk

City University of Hong Kong https://orcid.org/0000-0002-7315-1550

Lok Hin Law

City University of Hong Kong

Haoyun Su

City University of Hong Kong

Yang Liu

City University of Hong Kong

Liyan Wang

City University of Hong Kong

Se Weon Park

City University of Hong Kong

Huabing Liu

City University of Hong Kong

Wai Po Chong

Hong Kong Baptist University https://orcid.org/0000-0001-9640-199X

Article

Keywords: Glioblastoma, Theranostics, Intranasal Drug Delivery, CEST MRI, Liposomes, Amide Proton Transfer (APT)

Posted Date: November 4th, 2026

DOI: https://doi.org/10.21203/rs.3.rs-10897020/v1

License: This work is licensed under a Creative Commons Attribution 4.0 International License.
Read Full License

Additional Declarations: There is **NO** Competing Interest.

Abstract

Glioblastoma (GBM) treatment is limited by the blood-brain-barrier(BBB) and lack of non-invasive methods to track drug delivery and therapeutic response simultaneously. We developed a theranostic strategy utilizing multiparametric chemical exchange saturation transfer(CEST) MRI to guide the nose-to-brain delivery of mucus-penetrating liposomes encapsulating gemcitabine and iohexol(1:1; Gem/Ioh-Lipo). These multiple CEST contrast indicated drug-specific signals (gemcitabine 2.4 ppm, iohexol 4.3 ppm and liposome − 3.5 ppm), demonstrating that > 70% intranasal dose reached the frontal cortex from the olfactory bulb.Importantly, CEST at 4.3 ppm strongly correlated with tumor response($R^2 > 0.9$), indicating the prognostic value of image-guidance. Another CEST contrast (APTw at 3.5 ppm) indicated the tumor response, intranasal Gem/Ioh-Lipo produced an 8.6-fold tumor volume reduction versus drug-free liposomes ($P < 0.0001$). Controls showed a 55.9% increase in APTw signal in tumor ($P < 0.005$), indicating increased cellularity and proliferating cells, which were absent in treated animals. This CEST MRI-guided theranostic strategy enables non-invasive, real-time quantification of drug biodistribution and therapeutic efficacy for GBM, enabling precise treatment evaluation.

Introduction

Treatment for glioblastoma, a highly aggressive and malignant form of brain cancer, remains a formidable challenge in the field of oncology. Despite advances in surgical techniques, radiation therapy, and chemotherapy, the prognosis for patients diagnosed with glioblastoma remains poor [1]. By the restriction of the blood brain barrier (BBB), less than 0.1-2% of a therapeutic dose are able to enter the brain, depending on the molecule size [2–4]. The percentage of administered dose that arrives in the brain is relatively low due to the presence of the BBB, and tumors have abnormal vasculature and poor perfusion. This hampered the treatment efficacy[5]. Consequently, potent chemotherapeutics like gemcitabine, a prodrug that minimizes systemic side effects, are severely limited by conventional delivery routes. While Oral and intravenous administration is rendered largely ineffective by the BBB[6, 7], invasive alternatives such as intrathecal or convection-enhanced delivery risk severe neuronal damage, infection, and inflammation [8].

Beyond the challenge of delivery, a major bottleneck in current clinical assessment is the lack of imaging approaches capable of evaluating the actual percentage of the administered dose that reaches the brain. Current clinical paradigms rely on surrogate markers, such as systemic blood drug concentrations or delayed macroscopic changes in tumor size, neither of which accurately reflects immediate intracerebral drug penetrance or early molecular response[9–11].

Intranasal (IN) drug delivery systems have emerged as a promising alternative. These systems deliver drugs from the nose to the brain, bypassing the BBB and reducing the risk of damage associated with invasive methods [12, 13]. The transportation of drugs from the nasal cavity to the brain via several pathways, such as the intracellular pathway and extracellular pathway, through the glymphatic system and other pathways, such as systemic circulation [14]. The drug delivery efficacy of intranasal

administration can be up to 14.7 times higher than that of intravenous administration [15]. However, effective IN delivery must overcome rapid mucociliary clearance [16–21], enzymatic degradation [18, 22], and epithelial barriers [23].Previous studies have shown that high density coating with low molecular weight polyethylene glycol (PEG) can reduce liposomes adhesion to mucin fibers in the mucus mesh, resulting them to quickly penetrate through the low viscosity interstitial fluids between mucin fiber, further enhancing the efficiency of intranasal drug delivery [24–26], particularly for particles ranging in size from 100 to 500 nm[27]. Moreover, in addition to improving transport, PEGylation of nanoparticles enhances their stability in mucus, thereby facilitating their ability to diffuse through thick mucus layers and reach the underlying cells [28, 29]. In our previous study, we demonstrated the use of 10 mol % PEGylated liposome with size less than 200nm resulting in the best performance for CEST MRI guided intranasal drug delivery application [24].

To overcome the diagnostic bottleneck of tracking these therapeutics in vivo, we leverage multi-parametric Chemical Exchange Saturation Transfer (CEST) magnetic resonance imaging (MRI). CEST is a molecular imaging contrast mechanism in MRI, which detects both endogenous biomolecules and exogeneous CEST agents by probing the interaction between bulk water protons and labile solute protons [30]. By selectively saturating the exchangeable solute protons using RF irradiation, the saturation is transferred to the bulk water when the solute protons exchange with water protons, resulting in a slight attenuation of the water signal. In glioblastoma, both the complicated microenvironment and various biomolecules could contribute to the amide proton transfer weighted (APTw) contrast. Amide proton transfer (APT), one type of CEST contrast at 3.5 ppm from the water peak, can detect mobile protein/peptide concentrations and pH [31–33] and has been applied to studies of tumors and ischemic stroke [34–36]. APTw imaging has been demonstrated to be capable of detecting tumor aggressiveness, recurrence and can accurately differentiate active tumor from radiation necrosis [37–39]. Furthermore, multi-parametric CEST can holistically assess molecular treatment efficacy up to two days prior to observable changes in tumor size [40].In our previous study, we successfully demonstrated CEST can be used to monitor liposome-based nanomedicine, tracking its biodistribution and potentially the distribution of the free drug itself [30, 41].By combining multiple CEST contrast imaging, the drug delivery efficiency and therapeutic effect of the drug on glioblastoma can be monitored simultaneously, provide a comprehensive theranostic approach to glioblastoma treatment.

In this study, we leverage multi-parametric CEST MRI to create a theranostic platform for GBM. We modified 10% PEG liposomes to serve as intranasal nanocarriers and designed a 1:1 mixture of therapeutic liposomes (Gem-Lipo) and imaging contrast liposomes (Ioh-Lipo). Gemcitabine and iohexol are possibly interact each other and form macromolecular complex by hydrogen bond and π-π stacking between aromatic ring of each molecules [42]. The key advantage of this 1:1 imaging-to-drug ratio is that it enables the semi-quantitative imaging of the exact distribution of liposomes and drugs without chemical interaction and potentially altering the active chemotherapeutic. The distribution of the drug and liposomes will be tracked and monitored non-invasively by CEST MRI, while the therapeutic effect will be imaged by MRI for the size change of the tumor through T2-weighted and APT imaging. The therapeutic effect will be validated by immunohistology of brain slides, providing a comprehensive

assessment of this novel approach to glioblastoma treatment. This study represents a significant step forward in the development of more effective and less invasive treatment strategies for glioblastoma.

Results

In-Vitro and In-vivo Cytotoxicity Assessment

To access the effectiveness of the therapeutic effect on glioblastoma, in vitro cytotoxicity of gemcitabine, Gem-Lipo, gemcitabine/iohexol mixture, GEM-Lipo GEM/Ioh-Lipo, Co-GEM/Ioh-Lipo in U87 was examined with MTT assay (Fig. 1A, n = 3). Free gemcitabine, their liposomal form, and GEM/Ioh-Lipo showed a therapeutic effect on U87 cells. Treated cells showed an increase of cytotoxicity dependent to increase of the concentration of drug. The cell viability of U87 cells is decreased from 53.7% to 19.4% when the concentration of gemcitabine free drug is increased from 0.312 mg/mL to 5 mg/mL. For the GEM-Lipo, the cell viability of U87 cells is decreased from 100% to 34.9% when the concentration of GEM-Lipo is increased from 0.312 mg/mL to 5 mg/mL. For the GEM/Ioh-Lipo the cell viability of U87 cells is decreased from 100% to 34.9% when the concentration of GEM-Lipo is increased from 0.312 mg/mL to 5 mg/mL. While for the Co-GEM/Ioh-Lipo, the cell viability of U87 cells remain around 100% when the concentration of GEM-Lipo is increased from 0.312 mg/mL to 5 mg/mL.

Based on the in vitro cell cytotoxicity assay (Fig. 1A), 5 mg/ml gemcitabine resulted in the highest cell cytotoxicity to the U87 cell line. However, when we translated the same concentration of Gem-Lipo into in vivo glioblastoma therapy in Nod/SCID mice, the treated mice became fragile and the mortality rate increased after day 9 (Fig. 1B). To optimize the treatment dosage, we have performed a Kaplan-Meier survival analysis (survival curve) for four groups of different drug dosages for glioblastoma treatment, such as (a) 20 mg/kg Gem-Lipo daily treated group, (b) 10 mg/kg Gem-Lipo alternative day treated group, (c) 10 mg/kg Gem-Lipo daily treated group. In group (a), (c) the treated mice received a high mortality rate. We optimized the dose to obtain effective therapeutic outcome and high survival rate is 10 mg/kg Gem-Lipo group with alternative day treated group. Hence, we chose to use 5 mg/ml gemcitabine to prepare liposome for treatment, resulting in 2.5 mg/ml after mixing 1:1 with Ioh-Lipo, which remains around 50% cell cytotoxicity to the U87 cell line and a relatively high survival rate of animals.

Characterization of Theranostic Liposomes (Gem/Ioh-Lipo)

To establish a non-invasive theranostic platform for intranasal glioblastoma treatment, *in-vitro* CEST characterization was performed on the formulated liposomes: Gem-Lipo, Ioh-Lipo, a 1:1 mixture treatment liposome (Gem/Ioh-Lipo) and a co-encapsulated formulation (Co-Loaded Lipo). As shown in Fig. 2., we observed CEST contrast of 36.9 ± 0.4% at 4.3 ppm for free iohexol (328.3 mM in PBS at 7.0 pH) and 5.7 ± 0.2% at 2.3 ppm for free gemcitabine (19 mM in PBS at 7.0pH) when we acquired the z-spectrum at 1.0 μT, yielding a roughly 10-fold lower CEST signal. Consequently, the Gem-Lipo exhibited

only a CEST contrast of 3.4 ± 0.2% at 2.4 ppm (at 1.0 μT). Based on our preliminary dose optimization, the resulting therapeutic dose of gemcitabine is 2.5 mg/mL (equivalent to 9.5 mM). At this targeted concentration, the limited number of exchangeable protons renders the gemcitabine-derived CEST contrast at 2.3 ppm making it insufficient for in vivo tracking. We initially explored co-encapsulating both agents within the same nanocarrier (Co-Loaded Lipo). While this formulation yielded a strong CEST signal of 38.0 ± 1.0% at 4.3 ppm, it also produced an unexpected high contrast of 18.6 ± 6.8% at 1.0 ppm (corresponding to hydroxyl -OH protons). This indicates the induction intermolecular interactions or complex hydrogen bonding between iohexol and gemcitabine which reflected by the cytotoxicity assay that Co-Loaded Lipo compromise the therapeutic effect. Therefore, we designed the final treatment formulation as 1:1 mixture of individually loaded Gem-Lipo and Ioh-Lipo. Gem/Ioh-Lipo showed CEST contrast of 34.9%±0.3% at 4.3 ppm at 1.0 μT in-vitro. From the particle characterization and release study (Fig. 2A, D), Gem-Lipo, Ioh-Lipo showed a similar particle size, PDI, zetapotential, and release profile when comparing to our previous study for achieving similar mucus penetrating properties and biodistribution after intranasal administration. Therefore, the highly sensitive CEST contrast at 4.3 ppm derived from iohexol serves as the primary marker to accurately quantify the percentage of the intranasally administered dose that successfully reaches the brain. Ultimately, this strategic 1:1 mixture establishes a highly versatile, image-guided delivery platform, demonstrating that even if a primary therapeutic drug lacks intrinsic CEST contrast at clinical dosages, its precise in vivo biodistribution can still be reliably mapped by co-administering with our Ioh-Lipo.

In-Vivo Intranasal Liposome Delivery and Biodistribution Monitored by CEST MRI

To confirm the Treatment-Lipo delivery to the brain and monitor their biodistribution, 30μl Treatment-Lipo (Gem/Ioh-Lipo) and Control-Lipo (blank/Ioh-Lipo) was injected intranasally into each nostril of GBM mice model. The in-vivo MRI T2 image in coronal view, CEST Z-spectrum, $CEST_{LD}$ and CEST-map at the frontal lobe of GBM mouse model were acquired pre-injection and post-injection. As shown in Fig. 3A-H, in the treatment group, CEST contrasts at 4.3 ppm increased by 3.1 ± 0.8% and at -3.5 ppm increased by a percentage of 1.5 ± 0.4% in OB after injection compared to pre-injection. During this period, CEST contrasts at 4.3 ppm increased by a percentage of 1.4 ± 0.7% and at -3.5 ppm increased by a percentage of 1.3 ± 0.5% in FL. Comparably, in the control group, CEST contrasts at 4.3 ppm increased by a percentage of 2.6 ± 0.2% and at -3.5 ppm increased by a percentage of 0.6 ± 0.1% in OB after injection compared to pre-injection. During this period, CEST contrasts at 4.3 ppm increased by a percentage of 1.5 ± 0.7% and at -3.5 ppm increased by a percentage of 0.6 ± 0.2% in FL. Significant increases in CEST contrast at 4.3 ppm (indicating Iohexol) and at -3.5 ppm (indicating liposomal rNOE) were observed in both the olfactory bulb (OB) and the frontal lobe (FL) confirming successful nose-to-brain delivery.

The percentage dose of Iohexol (intraliposomal content) and liposomes reaching the tumor region from the OB were calculated by CEST contrast percentage differences between OB and the tumor region at 4.3 ppm and − 3.5 ppm (Fig. 3I). It shows a comparable drug delivery between the treatment and control

groups of over 70% of dose of iohexol and liposomes reaching the tumor, suggesting that the presence of gemcitabine did not substantially alter the delivery efficiency of the liposomes.

In-Vivo Therapeutic Efficacy and Tumor Response Monitoring by Multimodal MRI

To assess therapeutic efficacy, U87 GBM-bearing mice were randomized into treatment (IN Gem/Ioh-Lipo) and control (IN Blank/Ioh-Lipo) groups (n = 5 per group). Tumor growth and therapeutic response were monitored longitudinally using T2-weighted (T2w) MRI for tumor volume and CEST MRI for APT signal changes at 3.5 ppm as shown in Figs. 4 & 5. In the treatment group, the APTw CEST contrast remained relatively stable at 4.2 ± 0.3% throughout the two-week treatment period (4.5 ± 0.5%, 4.2 ± 0.6% and 4.0 ± 0.7% at 3.5ppm on Day 1, 7, 14 respectively). Conversely, in the control group, it showed a CEST contrast of 3.4 ± 1.0%, 4.1 ± 1.0% and 5.3 ± 0.6% at 3.5ppm on Day 1, 7, 14 respectively at the tumor region. the APTw of control group significantly increased by 0.8 ± 0.5% ($P = 0.027$) after 7 days, and significantly increased by 1.9 ± 0.8% ($P = 0.0039$) over two weeks. This increase in APT signal in control tumors is consistent with uncontrolled tumor proliferation and increased cellularity. The CEST also showed significant differences between the treatment group and the control group. In day 7, the APTw and MTR_{asym} contrast of control group is 1.0 ± 0.2% ($P < 0.01$) and 1.1 ± 0.6% ($P < 0.05$) higher than the treatment group respectively, while the APTw and MTR_{asym} contrast of control group is 2.4 ± 0.3% ($P < 0.001$) and 2.5 ± 0.7% ($P < 0.001$) higher than the treatment group in day 14. This shows the significant result of our treatment and indicates the tumor suppression effect of the treatment liposome in the treatment group.

In parallel, the tumor size showed a significant difference between treatment group and control group. As shown in Fig. 4E, over a 14-day period, the tumor volume in the treatment group increased by only 104.6 ± 48.6%. In contrast, tumors in the control group exhibited aggressive growth, with volumes increasing by 897.5 ± 478.1% ($P > 0.0001$), approximately 8.5 times their initial size. The significant increase in CEST contrast at 3.5 ppm of tumor region and the significant increase of the tumor size indicates the tumor growth in the control group, while the unchanged CEST contrast at 3.5 ppm of tumor region and the significant difference of the tumor size ($P > 0.0001$) between the treatment group and the control group indicates the efficacy of the intranasal treatment by the treatment-Lipo.

To evaluate the relationship between drug delivery and treatment effect, linear regression analyses were performed comparing imaging biomarkers, quantified drug dosage, and therapeutic outcomes (n = 5). First, the anatomical therapeutic response (percentage change in tumor size) was plotted against the in-vivo CEST signal difference before and after IN within the OB. A robust negative correlation was observed, demonstrating that higher early drug accumulation in OB strongly predicted eventual tumor suppression. Specifically, the CEST signal at 4.3 ppm (tracking iohexol) exhibited a highly significant correlation with the mitigation of tumor growth (Fig. 5A, $R^2 = 0.9572$). This result was further evaluated by analyzing the pixel-wise CEST signal distribution within the olfactory bulb. Subjects exhibiting a high

therapeutic effect displayed a distinct Post-IN rightward shift in CEST signal histograms at both 4.3 ppm and − 3.5 ppm (Fig. 5D, E), corresponding to substantial tumor growth suppression visible on longitudinal T_2-weighted MRI (Fig. 5H). Conversely, subjects with a low therapeutic effect demonstrated minimal histogram shifts (Fig. 5F, G) and larger residual tumor volumes (Fig. 5I). To assess target engagement and molecular therapeutic efficacy, the analytically determined percentage dose of iohexol delivered to the tumor was correlated with changes in the APTw signal, measured as the CEST difference at 3.5 ppm. A highly linear, negative correlation was observed between the delivered dose and the APTw signal (Fig. 5B, R^2 = 0.9433), indicating that higher intratumoral drug accumulation corresponded directly to a profound reduction in the APTw signal, an early biomarker for tumor cellularity. Finally, the anatomical therapeutic effect was directly compared to the percentage dose of the drug delivered into the tumor. Consistent with the imaging biomarkers, the iohexol dose showed a moderate negative linear correlation with anatomical tumor growth (Fig. 5C, R^2 = 0.6071). Notably, the correlation between the delivered drug dose and the molecular APTw signal changes (R^2 = 0.9433) was markedly stronger than its correlation with the anatomical tumor size difference (R^2 = 0.6071). These findings underscore that CEST MRI provides an earlier and significantly more sensitive assessment of therapeutic efficacy compared to conventional, macroscopic tumor sizing. By mapping localized drug delivery distributions, CESTRI can accurately forecast molecular target engagement and long-term treatment success before anatomical tumor growth appeared.

Histological Validation of Therapeutic Efficacy

Ex vivo histological analyses were performed on brain tissues collected on Day 14 from both treatment and control groups (n = 5 per group) to validate the in vivo MRI findings. Hematoxylin and Eosin (H&E) staining confirmed tumor presence and allowed assessment of overall tissue morphology. Quantitative analysis of DAPI-stained sections showed a significantly lower cell density in the tumors of the treatment group (2901 cells/mm3) compared to the control group (5361 cells/mm3), corresponding to a 45.89% reduction ($P < 0.001$, Fig. 6B, F). Immunohistochemical staining for Ki-67, a marker of cell proliferation, showed a significantly lower proliferation index in the treatment group (9.374 ± 1.22%) versus the control group (19.27 ± 1.51%). This represents a 61.30% reduction in proliferating cells ($P < 0.001$, Fig. 6C, G). Furthermore, TUNEL assays, which detect DNA fragmentation characteristic of apoptosis, showed a significantly higher apoptotic index in the tumors of treated mice (10.748 ± 1.54%) compared to controls (0.009 ± 0.005%) ($P < 0.0001$, Fig. 6D, H). We further analyze the correlations of APT contrast with cell density and proliferation. Both cell density and proliferation showed strong correlations with the APT signal (R^2 = 0.7120, P = 0.0021 and R^2 = 0.7824, P = 0.0007, respectively, Fig. 6I,J). This finding provides strong validation for APT imaging as a surrogate biomarker for tumor cellularity and proliferation in this GBM model and supports its utility in monitoring therapeutic response.

Moreover, we evaluated the spatial distribution of the therapeutic effect, ex vivo histopathological analysis was performed on tumor sections extracted on day 14 post-treatment (n = 5 per group). Immunofluorescence staining was obtained to analyse cellular proliferation (Ki-67) and apoptosis

(TUNEL) across three distinct spatial zones: the proximal region, the tumor core, and the distal region (Fig. 7E–H). Ki-67 staining (red) was lowest in the proximal region and became progressively higher toward the distal region. From the quantitative regional analysis (Fig. 7B), a significantly lower Ki-67 labeling index (LI) in the proximal region (11.33 ± 2.29%) compared to the distal region (27.92 ± 2.59%, $p < 0.01$). The tumor core showed intermediate proliferation (16.67 ± 2.37%), which was also significantly lower than the distal region ($p < 0.05$). Conversely, TUNEL staining (green) indicated that therapy-induced cell death was most concentrated near the region cloest to the injection site. The apoptotic index (Fig. 7C) was highest in the proximal region (21.66 ± 2.84%), showing a statistically significant elevation compared to both the tumor core (12.59 ± 1.48%, $p < 0.05$) and the distal region (9.83 ± 1.86%, $p < 0.05$). Meanwhile, the APT signal shows significantly lower in the proximal region (3.83 ± 1.27%) than that of the tumor core region (4.49 ± 1.46%, $p < 0.05$) and the distal region (5.11 ± 1.58%, $p < 0.01$), and the APT signal in the tumor core also shows significantly lower than that in the distal region ($p < 0.05$) (Fig. 7D). These findings demonstrate a robust apoptosis and proliferation inhibition in the proximal tumor region that gradually decrease toward the distal tumor microenvironment which can be sensitively detected by APTw imaging.

Discussions

The successful treatment of GBM hinges on overcoming two critical translational challenges: effectively bypassing the BBB to deliver therapeutic agents, and developing non-invasive, label-free methods to simultaneously monitor this delivery and real-time tumor response for prognosis. Regarding the first challenge, intravenous administration typically results in less than 0.1% of a therapeutic dose reaching the brain due to the highly restrictive nature of the BBB and the presence of active efflux pumps [2, 43–45]. In contrast, intranasal administration offers an alternative, routing therapeutics directly along the olfactory and trigeminal neural pathways bypassing the BBB to achieve significantly higher effective brain concentrations while minimizing systemic exposure. [12, 46]. However, to successfully exploit the IN route, nanocarriers must penetrate through the highly viscous nasal mucosa. Dense PEGylation has been extensively validated as a robust strategy to evade mucoadhesion and facilitate rapid mucus penetration [25, 47–53]. Building on our previous demonstrations that 10% PEGylated liposomes efficiently cross the nasal mucus to reach the brain [24, 26, 54]. we utilized this optimized 10% PEG liposomal formulation to maximize nose-to-brain delivery in this study.

The second major clinical challenge is tracking this targeted drug delivery and evaluating the subsequent treatment regimen. Amide Proton Transfer-weighted (APTw) CEST MRI has emerged as a powerful imaging biomarker for brain tumors [55, 56] ,capable of distinguishing tumor progression from treatment-induced necrosis [57, 58]. The APTw signal reduction after radiotherapy indicated a molecular tumor response, which claimed to be detected earlier than other commonly used MRI approaches[57]. Beyond endogenous proteins, CEST MRI can isolate exogenous agents at specific chemical shift offsets, such as glucose at 2 ppm [59–63], CT contrast agent like iohexol and iopamidol at 4.3 ppm [30, 64] and nanomaterial-based diamagnetic CEST agents including liposome at – 3.5 ppm [24]. In brain tumors, the complicated microenvironment and various molecules could contribute to the APTw contrast and rNOE,

resulting slightly different observations when we analyze CEST at 3.5 ppm and − 3.5 ppm independently, which APTw resulting hyperintense at 3.5 ppm reflecting protein synthesis and high cellularity while rNOE resulting hypointense reflecting mobile lipids and macromolecule changes in tissue. By mapping these distinct contrasts, our multi-offset CEST MRI platform uniquely achieves the simultaneous, real-time tracking of exogenous liposomal delivery (-3.5 ppm and 4.3 ppm) and early molecular tumor progression (3.5 ppm) within a single comprehensive imaging framework.

In this study, we demonstrated CEST MRI guided glioblastoma treatment using intranasal liposome. Gemcitabine is chosen to load into 10% PEG liposome as a prodrug, which activates the anti-cancer mechanism after entering the cancer cell [65]. While the standard-of-care drug temozolomide was considered, its known susceptibility to rapid hydrolytic degradation in aqueous environments significantly compromises its stability and therapeutic effect in the liposomal formulations [66]. To establish the effective treatment dose for our *in-vivo* model, we translated the established clinical IV gemcitabine regimen (1000 mg/m² administered on Days 1 and 8 of a 21-day cycle) to a rodent equivalent dosage of approximately 30 mg/kg. Since intranasal administration directly bypasses the BBB, yielding a substantially higher brain bioavailability compared to systemic IV injection, we were able to optimize our treatment protocol, ensuring sufficient therapeutic concentrations reached the tumor core while potentially minimizing off-target systemic toxicities.

The clinical translation of this localized delivery strategy relies on the ability to non-invasively track the nanocarrier and simultaneously monitor the tumor's response. To achieve this multiparametric imaging capability without compromising drug efficacy, we designed our final formulation as a 1:1 mixture of separately loaded therapeutic liposomes (Gem-Lipo) and imaging liposomes (Ioh-Lipo). This separate-nanocarrier design was fundamentally driven by our in vitro cytotoxicity assays (Fig. 1a). When gemcitabine and iohexol were co-encapsulated within the same liposome (Co-GEM/Ioh-Lipo) or mixed as free solutions, the cytotoxic efficacy against U87 cells was severely suppressed. This compromised efficacy is probably caused by spontaneous molecular complexation within the intraliposomal core, characterized by extensive hydrogen bonding networks and π-π stacking cooperativity between gemcitabine and iohexol[42]. By encapsulating the agents into separate liposomes, we successfully insulated the active chemotherapeutic from the contrast agent. This approach preserved the potent cytotoxicity of gemcitabine while establishing a highly robust, image-guided delivery platform. It allows us to semi-quantitatively map the precise biodistribution of the drug vehicle (via the Ioh-Lipo) while concurrently tracking early molecular changes in the tumor microenvironment (via the APTw signal). By linking spatial drug delivery metrics to molecular target engagement, this image-guided platform can semi-quantitatively predict long-term anatomical treatment effects, empowering clinicians to proactively tailor and greatly enhance personalized treatment regimens.

For the in vivo experiment, we confirmed the successful nose-to-brain delivery of our treatment liposome (GEM/Ioh-Lipo) and control liposome (Blank/Ioh-Lipo). We acquired CEST MRI pre-IN and post-IN for both the treatment group and the control group. By co-injection of the Ioh-Lipo, we were able to non-invasively track the nanocarrier delivery into the olfactory bulb and subsequent distribution to the tumor-

bearing frontal lobe using the unique CEST contrast at 4.3 ppm for intraliposomal agent distribution and − 3.5 ppm for liposome distribution. This indicates that both the treatment liposome and the control liposome are delivered to the brain with comparable efficacy and distribution. Notably, we observed the liposomal distribution by assessing the CEST map at -3.5 ppm (Fig. 3). The liposomes are distributed surrounding the tumor region. This indicates that the liposomes might not penetrated into the core of the tumor, which results in a limited therapeutic outcome. Further investigation of delivering the drug liposome into the core of the tumor can be done for a more effective therapeutic outcome, such as shrinkage of the tumor.

In this study, we demonstrate the therapeutic efficacy of the Gem/Ioh-Lipo to complete the theranostic loop. By comparing the APTw and rNOE CEST contrast and CEST map at 3.5 ppm and − 3.5 ppm (Figs. 4 & 5), we observed CEST contrast at 3.5 ppm (APTw) remained at a similar level for the entire treatment duration (two weeks) in the treatment group, while the APTw of the control group significantly increased by 2 times ($P < 0.0039$) over two weeks. This trend was also seen in the tumor size. The tumor remained at low volume for entire treatment duration in the treatment group, while the tumor size increased for more than 8-fold ($P < 0.0001$) in the same time interval for the control group. These two results indicate that the treatment liposomes show the therapeutic outcome of suppressing the tumor growth. From our data, the SEM of CEST and MTRasym are both < 1.0%. The CEST signal specific indicate the contrast at specific offset, while MTRasym is obtained from the difference between the CEST contrast of 3.5 and − 3.5 ppm. CEST shows an accurate value of specific offset while MTRasym is the clinical protocol for assessing tumor progression. From our result, both values showed a low SEM indicate the accuracy of our MRI scanning.

We also validated the relationship between drug delivery and treatment effect (Fig. 6). The robust correlations shown in our data demonstrate the theranostic utility of multiple CEST MRI for intranasal drug delivery. Our results reveal that non-invasive tracking of early CEST signal changes, specifically the CEST signal at 4.3 ppm and the distinct rightward shifts in pixel-wise signal distribution (histograms) in the OB, can reliably predict long-term anatomical treatment outcomes (tumor suppression). Notably, the high correlation between CEST signal at 4.3 ppm in OB and tumor size change ($R^2 = 0.9572$) underscores that early quantification of drug uptake at the primary anatomical gateway to the brain is sufficient to forecast distal therapeutic success. Furthermore, by directly correlating the percentage of dose of the drug delivered with the APTw signal (3.5 ppm), we validated CEST MRI as a highly sensitive tool for monitoring molecular therapeutic efficacy. The near-perfect correlation ($R^2 = 0.9433$) between the intratumoral dose and the reduction in the APTw signal confirms that the delivered agents successfully engaged their targets within the glioblastoma, altering the tumor's molecular microenvironment prior to observable macroscopic changes. Importantly, a direct comparison of these metrics revealed that the correlation between the delivered drug dose and early molecular APTw signal changes ($R^2 = 0.9433$) was markedly stronger than its correlation with long-term anatomical tumor size differences ($R^2 = 0.6071$). This discrepancy indicates that CEST MRI provides a significantly earlier and more sensitive evaluation of therapeutic efficacy than conventional macroscopic tumor sizing. These findings support the

integration of multi-offset CEST MRI into clinical workflows, enabling clinicians to simultaneously verify early drug delivery, assess molecular treatment efficacy, and predict long-term anatomical outcomes, thereby facilitating real-time, personalized adjustments to neuro-oncological treatment regimens for precise therapy and prognosis.

We further validate the in vivo APTw signal with the ex vivo histological markers of cell density, proliferation and apoptosis. In the histology, we can observe that the cell density and Ki-67 labelling index are significantly lower in the treatment group than that in the control group ($P < 0.001$) (Fig. 6F, G). The cell density and the Ki-67 labelling index of the treatment group were 54.11% and 51.35% lower than that of the control group respectively. The major mechanism of action of gemcitabine is inhibiting DNA synthesis and enhancing its own effects through the activation of deoxycytidine kinase and caspase signaling pathways, ultimately leading to apoptosis of proliferating cancer cells [67, 68], which can be validated by the apoptosis index which is significantly higher in the treatment group than that in the control group ($P < 0.0001$) (Fig. 6H). The over 50% lower Ki-67 labelling index of the treatment group indicated the decrease of proliferating glioblastoma cells, which ultimately resulted in a decrease in cell density in the tumor region in the treatment group. The strong positive correlations of the APT signal with cell density and proliferation further support that the decrease in APT was sensitive to detect the reduction of tumor cell density and proliferation by the IN treatment of Gem-Lipo. This result validates the therapeutic outcome of tumor growth suppression, as shown in the CEST result. It suggests that APTw-CEST MRI can provide a molecular-level assessment of treatment efficacy, potentially enabling clinicians to gauge patient response much earlier than conventional anatomical imaging and to adjust therapeutic strategies accordingly. We also analyzed the therapeutic outcomes in different region of the tumor to provide critical microenvironmental validation of the distance-dependent treatment efficacy (Fig. 7). The higher apoptotic induction and proliferation inhibition observed in the proximal tumor region indicate that the intranasally administered treatment-Lipo achieved high therapeutic effect at the primary site of entry. However, the progressive increase in proliferating index (Ki-67) and the decrease in apoptotic index (TUNEL) toward the distal region highlight a major pharmacological hurdle: the limited deep-tissue penetration and heterogeneous distribution of therapeutics within the dense solid tumor microenvironment. From a theranostic perspective, these findings emphasize the critical needs of advanced imaging modalities, such as multiple CEST MRI, to map intra-tumoral drug distribution in real-time. Furthermore, this finding also suggested the future direction of development of nanocarriers to enhance the diffusive or tumor penetration properties to ensure homogeneous drug distribution and better therapeutic effect.There are several limitations in our study. The distinct CEST contrasts for tracking the liposomal distribution (-3.5 ppm), tracking the drug distribution (4.3 ppm) and monitoring the therapy (3.5 ppm) have different optimal imaging parameters. APT is more prominent at high B_1 power, while rNOE is more prominent at low B_1 power. Therefore, the therapeutic outcome at 3.5 ppm and drug distribution at 4.3 ppm need a high B_1 power to have the optimized CEST contrast, while the liposomal distribution at -3.5 ppm requires a low B_1 power to have the optimized CEST contrast. Further optimization of the MRI pulse sequence is needed to create a streamlined protocol for potential clinical translation. Additionally, drugs delivered *via* the intranasal route, with agents reaching the brain within

30–60 minutes, requires a fast and efficient imaging window. Future work should focus on accelerating the CEST acquisition protocol. Finally, while we demonstrated profound tumor suppression, complete tumor regression was not achieved, possibly due to the limited penetration of liposomes into the tumor core as suggested by our CEST maps. Future iterations of this platform could incorporate strategies to enhance tumor penetration, such as targeting ligands or the use of focused ultrasound, to further improve therapeutic outcomes.

In conclusion, we developed a CEST MRI-guided glioblastoma treating intranasal liposome. Our treatment-Lipo has CEST contrast at 4.3 ppm and − 3.5 ppm in vitro, indicating the intraliposomal drug/CT agent encapsulation and phospholipid bilayer of liposome, respectively. By monitoring this unique CEST contrast in vivo, we achieved the tracking and monitoring of treatment-Lipo distribution inside the brain and drug delivery efficacy from nose to brain. Meanwhile, by monitoring CEST contrast at 3.5 ppm and T2w images, the treatment effect and tumor progression are simultaneously examined. The treatment-Lipo shows a suppression effect on glioblastoma which is validated by the H&E histology, Ki-67, and the TUNEL immunohistology.

Methods

Materials

Gemcitabine were purchased from Sigma-Aldrich (St. Louis, MO, USA). CT Contrast agents (Iohexol) were purchased from GE Healthcare Life Sciences (Pittsburg, PA). 1,2-distearoyl-sn-glycero-3-phosphocholine (DSPC), and 1,2-distearoyl-sn-glycero-phosphoethanolamine poly (ethylene glycol)2000 (DSPE-PEG-2000) were purchased from Avanti Polar Lipids, Inc. (Alabaster, AL). Sephadex G50 columns were bought from GE Healthcare Life Sciences (Pittsburg, PA). U87 cell line was purchased from ATCC (Manassas, VA). Eagle's Minimum Essential Medium (EMEM), phosphate-buffered saline (PBS, pH 7.4), fetal bovine serum (FBS), penicillin-streptomycin and trypsin were all purchased from Gibco, Invitrogen (California, CA). All the chemicals and solvents used in the study were of analytical grade and purchased from Sigma-Aldrich (St. Louis, MO, USA). Deionized water was used throughout the experiments.

Drug/CT agent Solution and Drug/CT agent Loaded Liposome Preparation

For gemcitabine solution, gemcitabine hydrochloride (MW = 299.66 g/mol) was dissolved in PBS solution with a concentration of 5 mg/mL in 7.0 pH. For CT agent iohexol solution, 500µl iohexol (MW = 821.138 g/mol) solution with concentration of 647 mg/ml was dissolved in 700µl distilled water in 7.0 pH to prepare a 328.3mM iohexol solution. For gemcitabine and iohexol mixture, 5mg/mL gemcitabine solution and 328.3mM iohexol solution are mixed in 1:1 ratio.

Gemcitabine encapsulated liposome (Gem-Lipo), iohexol encapsulated liposome (Ioh-Lipo), and co-loaded gemcitabine and iohexol liposome (Co-Gem/Ioh-Lipo) was prepared through thin film hydration[69], and extrusion method using a formulation of DSPC:cholesterol:DSPE-PEG2000:rhodamine

= 50:40:10:0.18 for 10% PEG Ioh-Lipo as described in our previous study. The lipid mixture was dissolved in chloroform and evaporated to form a dry homogeneous thin film layer by a rotary evaporator (Heidolph, Schwabach, Germany). The lipid film was then rehydrated with the gemcitabine, iohexol solution or their mixture at a temperature higher than the transition temperature of the lipid, and sonicated for 30 min to form large multilamellar liposomes (MLVs). The solution was finally extruded through 400 nm polycarbonate membranes for 15 times then through 200 nm polycarbonate membranes for another 15 times to obtain the resultant liposome with size < 150 nm. The unloaded drug of the resultant liposome solution was filtered through Sephadex G-50 gel columns twice before imaging. Mixed gemcitabine loaded liposome and iohexol loaded liposome (Gem/Ioh-Lipo) is prepared by mixing Gem-Lipo and Ioh-Lipo in 1:1 ratio.

Liposome Characterization and Drug Release Profile

The size, polydispersity index (PDI) and surface charge of liposomes were measured by dynamic light scattering (DLS) at room temperature by Zetasizer (Malvern Instruments, UK). The particle concentration was measured by Nanosight (Malvern Instruments, UK).

The loading of gemcitabine and iohexol in liposomes was estimated by measuring the UV absorbance at 270nm and 245 nm using UV-VIS spectrometer (PerkinElmer, MA, USA). Gem-Lipo and Ioh-Lipo were treated with Triton X-100 solution to completely release the Gemcitabine and iohexol payload, diluted to proper concentration, followed by UV measurements. The concentration was then determined by the calibration curves of gemcitabine and iohexol solutions with known concentrations.

Gemcitabine and iohexol release from liposomes were studied using a dialysis method. Dialysis bags were soaked before use in distilled water at room temperature for 12 h to remove the preservative, followed by rinsing thoroughly in distilled water. The release experiments were done immediately after the preparation of liposomes. The liposome stock solution was diluted 10 times. The resulting liposomes suspension 500 µl was taken to dialysis bag (cut off molecular weight: 3000/5000) and immersed into 10 mL PBS solution. The sac was hung inside a conical flask with the help of a glass rod so that the portion of the dialysis sac with the formulation dipped into the buffer solution. The flask was kept on a magnetic stirrer and stirring was maintained at 100 rpm at 37°C with a thermostatic control. 1 mL supernatant was taken out and re-supplemented with fresh PBS at 0.25, 0.5, 1, 2, 4, 6, 9, 24, 48 h., followed by UV measurements at 270 nm and 245 nm.

Cell Preparation

Human glioblastoma cells (U87) were cultivated in Dulbecco Modified Eagle Medium (DMEM) containing 10% fetal bovine serum (FBS) and 1% Penicillin-Streptomycin. The cell cultures were maintained at 37°C in a > 95% humidified atmosphere of 5% CO_2 in air with media changes on alternate days.

Cytotoxicity Assays

Drug solution and 10% PEG drug loaded-Lipo were tested in U87 cell line. Five concentrations of each drug and drug loaded-liposome were tested: Gemcitabine, Gemcitabine/Iohexol mixture, GEM-Lipo

GEM/Ioh-Lipo, Co-Lipo-GEM/Ioh. 5×10^3 cells were cultured and seeded with 100 µL into 96-well plates 24 h prior to treatment. After drug solution and drug loaded liposome addition, the cells were incubated for 72 hours. The liposome mixture in the culture plate is extracted and washed by PBS before cellular toxicity quantification by MTT assay. Cytotoxicity of drug solution and drug loaded liposome are measured by the UV absorbance reading by microplate reader (Molecular Devices, CA, USA). Cytotoxicity was expressed as percentage of the Relative Growth Rate (RGR) by the equation:

RGR = (Dsample/Dcontrol)/100

where Dsample and Dcontrol are the absorbance of the test samples and the negative controls, respectively.

Animal Model and Dosing Optimization

All animal procedures were approved by the Department of Health (DH) of Hong Kong, in compliance with the Animals (Control of Experiments) Ordinance (Chap. 340). The experiments were conducted at the City University of Hong Kong's Laboratory Animal Research Unit (LARU), where animals were maintained in a pathogen-free facility with free access to food and water.

For the tumor-bearing mice model, NOD/SCID mice (8-week-old) was used for brain tumor injection to generate xenografts. Prior to xenotransplantation, U87 tumor cells were analyzed for cell count and cell viability using. U87 cells (0.5×10^6/3µL) were implanted at the following coordinates from bregma: anteroposterior = + 1.5 mm, lateral + 1.5 mm, dorsoventral − 1.2 mm. Each mouse was inoculated with U87 tumor cells. The injection consisted of 0.5×10^6 cells suspended in 3µL of cell culture media. Tumors development is measured 3, 7, 10, 14 days post-xenotransplantation.

Tumor-bearing mice are divided into 4 regimen groups, (a) 20 mg/kg Gem-Lipo daily treated group, (b) 10 mg/kg Gem-Lipo alternative day treated group, (c) 10 mg/kg Gem-Lipo daily treated group (d) control group. Mice survival are monitored for 14-day-treatment with the 4 regimen groups by Kaplan-Meier curves.

In-vivo MRI for drug distribution and anticancer effect

T2-weighted (T2W) and CEST images were acquired pre-treatment, 0.5h after intranasal injection of mixed-Lipo and monitor on 14, 21, 28th day. Treated mouse was hold for 30 mins to ensure liposomes were transported and penetrated into the olfactory bulb. The in-vivo MRI images for intranasal administration experiments at the olfactory bulb of mice were acquired on a horizontal bore 3 T Bruker BioSpec system (Bruker, Ettlingen, Germany) equipped with one 82 mm quadrature volume resonator as a transmitter and a single surface coil as a receiver. The T2 weighted image and CEST data in coronal view were acquired. The CEST sequence was RARE sequence with a CW pre-saturation module. The parameters were set as followings: slice thickness = 2 mm, field of view (FOV) = 16 × 16 mm2, image size = 64 × 64, RARE factor = 32, TR/TE = 5000/5 ms. B1 was varied as: 0.6, tsat = 3 s,CEST frequency varied from − 15 to + 15 ppm, with a step of 0.2 ppm between − 6 to 6 ppm, a step of 1 ppm between ± 6

and ± 15 ppm and extra acquisition points on ± 2.1, ± 2.25, ± 2.3, ± 2.35, ± 2.45, ± 2.5, ± 3.3, ± 3.45, ± 3.5, ± 3.55, ± 3.7, ± 4.1, ± 4.25, ± 4.3, ± 4.35, ± 4.5 ppm and ± 20 ppm. Three M0 images at 200 ppm were acquired for normalization.

MRI Data Analysis

The data were processed by custom-written MatLab (Mathworks, Natick, MA) code as described in our previous study [23]. In brief, after acquiring CEST data, the raw Z-spectra (Z) were formed, the B0 correction was performed on a pixel-wise basis. Lorentzian difference analysis was adopted for calculating CEST contrasts.

Histological Analysis

On Day 14, mice were euthanized and transcardially perfused with PBS followed by 4% paraformaldehyde (PFA). Brains were harvested, post-fixed in 4% PFA, and cryoprotected in a 30% sucrose solution. Serial coronal sections (20 μm) were prepared using a cryostat. Sections were stained with Hematoxylin and Eosin (H&E) for general morphology. For immunohistochemistry, sections were stained for Ki-67 (proliferation marker; Thermofisher) and subjected to a terminal deoxynucleotidyl transferase dUTP nick end labeling (TUNEL) assay (apoptosis marker; Thermofisher). All sections were counterstained with DAPI for nuclear visualization. Images were acquired using a fluorescence microscope, and quantitative analysis (cell density, Ki-67 labeling index, apoptosis index) was performed using ImageJ software on three representative sections per tumor.

Statistical Analysis

All quantitative data are presented as mean ± standard deviation (SD). Statistical analyses were performed using GraphPad Prism software. Comparisons of tumor volume and CEST contrast changes over time between the treatment and control groups were performed using a two-way ANOVA with Sidak's multiple comparisons test. Comparisons of histological data between the two groups were performed using an unpaired two-tailed t-test. The correlation between APTw signal and histological metrics was assessed using Pearson correlation analysis. A P-value < 0.05 was considered statistically significant.

Declarations

Author Contribution

Lok Hin Law: Conceptualization, Methodology, Formal analysis, Investigation, Data curation, Writing – original draft, Writing – review & editing, Visualization. **Haoyun Su**: Investigation, Writing – review & editing, Visualization. **Yang Liu**: Software. **Liyan Wang**: Investigation. **Seweon Park**: Investigation. **Huabing Liu**: Investigation. **Wai Po Chong**: Investigation. **Kannie W.Y. Chan**: Conceptualization, Methodology, Writing – review & editing, Visualization, Supervision, Project administration, Funding acquisition.

Acknowledgments

Authors would like to acknowledge the funding supports from Research Grants Council of the Hong Kong Special Administrative Region, China (11105326, 11206325, 11102218, 11200422, CityUHK RFS2223-1S02); HMRF (21222621); MHKJS (MHP/076/23); InnoHK initiative of the Innovation and Technology Commission of the Hong Kong Special Administrative Region Government - Hong Kong Centre for Cerebro-cardiovascular Health Engineering; City University of Hong Kong (7030012, 9678372, 9609321 and 9610616), Tung Biomedical Sciences Centre; State Key Laboratory of Terahertz and Millimeter Waves

Data Availability

All data supporting the findings of this study are available within the Source Data file. Source data are provided with this paper.

References

1. W. Wu, J.L. Klockow, M. Zhang, F. Lafortune, E. Chang, L. Jin, Y. Wu, H.E. Daldrup-Link, Glioblastoma multiforme (GBM): An overview of current therapies and mechanisms of resistance, Pharmacological research, 171 (2021) 105780.
2. R. Bajracharya, A.C. Caruso, L.J. Vella, R.M. Nisbet, Current and emerging strategies for enhancing antibody delivery to the brain, Pharmaceutics, 13 (2021) 2014.
3. D. Wu, Q. Chen, X. Chen, F. Han, Z. Chen, Y. Wang, The blood–brain barrier: Structure, regulation and drug delivery, Signal transduction and targeted therapy, 8 (2023) 217.
4. W.M. Pardridge, Blood–brain barrier delivery, Drug discovery today, 12 (2007) 54–61.
5. A. Bhowmik, R. Khan, M.K. Ghosh, Blood brain barrier: a challenge for effectual therapy of brain tumors, BioMed research international, 2015 (2015) 320941.
6. R. Pandit, L. Chen, J. Götz, The blood-brain barrier: Physiology and strategies for drug delivery, Advanced drug delivery reviews, 165 (2020) 1–14.
7. W.A. Banks, From blood–brain barrier to blood–brain interface: new opportunities for CNS drug delivery, Nature reviews Drug discovery, 15 (2016) 275–292.
8. G.C. Terstappen, A.H. Meyer, R.D. Bell, W. Zhang, Strategies for delivering therapeutics across the blood–brain barrier, Nature Reviews Drug Discovery, 20 (2021) 362–383.
9. A. Quick, D. Patel, M. Hadziahmetovic, A. Chakravarti, M. Mehta, Current therapeutic paradigms in glioblastoma, Reviews on Recent Clinical Trials, 5 (2010) 14–27.
10. J.D. Bernstock, S.E. Gary, N. Klinger, P.A. Valdes, W. Ibn Essayed, H.E. Olsen, G. Chagoya, G. Elsayed, D. Yamashita, P. Schuss, Standard clinical approaches and emerging modalities for glioblastoma imaging, Neuro-Oncology Advances, 4 (2022) vdac080.

11. A.C. Tan, D.M. Ashley, G.Y. López, M. Malinzak, H.S. Friedman, M. Khasraw, Management of glioblastoma: State of the art and future directions, CA: a cancer journal for clinicians, 70 (2020) 299–312.
12. T.P. Crowe, M.H.W. Greenlee, A.G. Kanthasamy, W.H. Hsu, Mechanism of intranasal drug delivery directly to the brain, Life sciences, 195 (2018) 44–52.
13. J.J. Lochhead, R.G. Thorne, Intranasal delivery of biologics to the central nervous system, Advanced drug delivery reviews, 64 (2012) 614–628.
14. K. Selvaraj, K. Gowthamarajan, V.V.S.R. Karri, Nose to brain transport pathways an overview: Potential of nanostructured lipid carriers in nose to brain targeting, Artificial cells, nanomedicine, and biotechnology, 46 (2018) 2088–2095.
15. S. Ahmad, I. Khan, J. Pandit, N.A. Emad, S. Bano, K.I. Dar, M.M.A. Rizvi, M.D. Ansari, M. Aqil, Y. Sultana, Brain targeted delivery of carmustine using chitosan coated nanoparticles via nasal route for glioblastoma treatment, International journal of biological macromolecules, 221 (2022) 435–445.
16. R. Bansil, B.S. Turner, Mucin structure, aggregation, physiological functions and biomedical applications, Current opinion in colloid & interface science, 11 (2006) 164–170.
17. S.K. Lai, Y.-Y. Wang, D. Wirtz, J. Hanes, Micro-and macrorheology of mucus, Advanced drug delivery reviews, 61 (2009) 86–100.
18. M.A. Sarkar, Drug metabolism in the nasal mucosa, Pharmaceutical research, 9 (1992) 1–9.
19. M.S. Ali, J.P. Pearson, Upper airway mucin gene expression: a review, The Laryngoscope, 117 (2007) 932–938.
20. R.M. Mainardes, M.C. Urban, P.O. Cinto, M.V. Chaud, R.C. Evangelista, M.D. Gremiao, Liposomes and micro/nanoparticles as colloidal carriers for nasal drug delivery, Current drug delivery, 3 (2006) 275.
21. K. Saketkhoo, A. Januszkiewicz, M.A. Sackner, Effects of drinking hot water, cold water, and chicken soup on nasal mucus velocity and nasal airflow resistance, Chest, 74 (1978) 408–410.
22. A. Minn, S. Leclerc, J.-M. Heydel, A.-L. Minn, C. Denizot, M. Cattarelli, P. Netter, D. Gradinaru, Drug transport into the mammalian brain: the nasal pathway and its specific metabolic barrier, Journal of drug targeting, 10 (2002) 285–296.
23. E.V. Koch, S. Bendas, K. Nehlsen, T. May, S. Reichl, A. Dietzel, The path from nasal tissue to nasal mucosa on chip: Part 2—advanced microfluidic nasal in vitro model for drug absorption testing, Pharmaceutics, 15 (2023) 2439.
24. L.H. Law, J. Huang, P. Xiao, Y. Liu, Z. Chen, J.H. Lai, X. Han, G.W. Cheng, K.-H. Tse, K.W. Chan, Multiple CEST contrast imaging of nose-to-brain drug delivery using iohexol liposomes at 3T MRI, Journal of Controlled Release, 354 (2023) 208–220.
25. J.S. Suk, Q. Xu, N. Kim, J. Hanes, L.M. Ensign, PEGylation as a strategy for improving nanoparticle-based drug and gene delivery, Advanced drug delivery reviews, 99 (2016) 28–51.

26. T. Yu, K.W. Chan, A. Anonuevo, X. Song, B.S. Schuster, S. Chattopadhyay, Q. Xu, N. Oskolkov, H. Patel, L.M. Ensign, Liposome-based mucus-penetrating particles (MPP) for mucosal theranostics: demonstration of diamagnetic chemical exchange saturation transfer (diaCEST) magnetic resonance imaging (MRI), Nanomedicine: Nanotechnology, Biology and Medicine, 11 (2015) 401–405.
27. S.K. Lai, D.E. O'Hanlon, S. Harrold, S.T. Man, Y.-Y. Wang, R. Cone, J. Hanes, Rapid transport of large polymeric nanoparticles in fresh undiluted human mucus, Proceedings of the National Academy of Sciences, 104 (2007) 1482–1487.
28. D. Makharadze, L.J. Del Valle, R. Katsarava, J. Puiggalí, The art of PEGylation: from simple polymer to sophisticated drug delivery system, International journal of molecular sciences, 26 (2025) 3102.
29. M. Piñol-Cancer, L. Fernández-Méndez, J. Carrillo-Romero, A. Urkola-Arsuaga, M. Azkargorta, F. Elortza, F. Goñi-de-Cerio, C. García-Mouton, C.M.-P. de Alejo, E. Ismalaj, The role of PEGylation in the pulmonary delivery of antifibrotic liposomal therapies, Journal of Controlled Release, (2025) 114134.
30. P.C. Van Zijl, N.N. Yadav, Chemical exchange saturation transfer (CEST): what is in a name and what isn't?, Magnetic resonance in medicine, 65 (2011) 927–948.
31. S. Aime, L. Calabi, L. Biondi, M. De Miranda, S. Ghelli, L. Paleari, C. Rebaudengo, E. Terreno, Iopamidol: Exploring the potential use of a well-established x-ray contrast agent for MRI, Magnetic Resonance in Medicine: An Official Journal of the International Society for Magnetic Resonance in Medicine, 53 (2005) 830–834.
32. P.Z. Sun, A.G. Sorensen, Imaging pH using the chemical exchange saturation transfer (CEST) MRI: correction of concomitant RF irradiation effects to quantify CEST MRI for chemical exchange rate and pH, Magnetic Resonance in Medicine: An Official Journal of the International Society for Magnetic Resonance in Medicine, 60 (2008) 390–397.
33. L.Q. Chen, C.M. Howison, J.J. Jeffery, I.F. Robey, P.H. Kuo, M.D. Pagel, Evaluations of extracellular pH within in vivo tumors using acidoCEST MRI, Magnetic resonance in medicine, 72 (2014) 1408–1417.
34. C.K. Jones, M.J. Schlosser, P.C. Van Zijl, M.G. Pomper, X. Golay, J. Zhou, Amide proton transfer imaging of human brain tumors at 3T, Magnetic Resonance in Medicine: An Official Journal of the International Society for Magnetic Resonance in Medicine, 56 (2006) 585–592.
35. J. Zhou, J.O. Blakeley, J. Hua, M. Kim, J. Laterra, M.G. Pomper, P.C. Van Zijl, Practical data acquisition method for human brain tumor amide proton transfer (APT) imaging, Magnetic Resonance in Medicine: An Official Journal of the International Society for Magnetic Resonance in Medicine, 60 (2008) 842–849.
36. S. Goerke, Y. Soehngen, A. Deshmane, M. Zaiss, J. Breitling, P.S. Boyd, K. Herz, F. Zimmermann, K.D. Klika, H.P. Schlemmer, Relaxation-compensated APT and rNOE CEST-MRI of human brain tumors at 3 T, Magnetic resonance in medicine, 82 (2019) 622–632.
37. J.E. Park, H.S. Kim, K.J. Park, S.J. Kim, J.H. Kim, S.A. Smith, Pre-and posttreatment glioma: comparison of amide proton transfer imaging with MR spectroscopy for biomarkers of tumor proliferation, Radiology, 278 (2016) 514–523.

38. K. Sagiyama, T. Mashimo, O. Togao, V. Vemireddy, K.J. Hatanpaa, E.A. Maher, B.E. Mickey, E. Pan, A.D. Sherry, R.M. Bachoo, In vivo chemical exchange saturation transfer imaging allows early detection of a therapeutic response in glioblastoma, Proceedings of the National Academy of Sciences, 111 (2014) 4542–4547.
39. J. Zhou, H.Y. Heo, L. Knutsson, P.C. van Zijl, S. Jiang, APT-weighted MRI: techniques, current neuro applications, and challenging issues, Journal of Magnetic Resonance Imaging, 50 (2019) 347–364.
40. S.-W. Park, J.H. Lai, X. Han, V.W. Leung, P. Xiao, J. Huang, K.W. Chan, Preclinical application of CEST MRI to detect early and regional tumor response to local brain tumor treatment, Pharmaceutics, 16 (2024) 101.
41. X.Y. Zhang, F. Wang, H. Li, J. Xu, D.F. Gochberg, J.C. Gore, Z. Zu, Accuracy in the quantification of chemical exchange saturation transfer (CEST) and relayed nuclear Overhauser enhancement (rNOE) saturation transfer effects, NMR in biomedicine, 30 (2017) e3716.
42. X. Cheng, Q. Ji, D. Sun, J. Zhang, X. Chen, H. He, S. Li, S. Yang, L. Zhang, A comparative study on adsorption behavior of iodinated X-ray contrast media iohexol and amidotrizoic acid by magnetic-activated carbon, Environmental Science and Pollution Research, 29 (2022) 45404–45420.
43. R.W. Robey, K.M. Pluchino, M.D. Hall, A.T. Fojo, S.E. Bates, M.M. Gottesman, Revisiting the role of ABC transporters in multidrug-resistant cancer, Nature Reviews Cancer, 18 (2018) 452–464.
44. P. Ballabh, A. Braun, M. Nedergaard, The blood–brain barrier: an overview: structure, regulation, and clinical implications, Neurobiology of disease, 16 (2004) 1–13.
45. T.P. Crowe, W.H. Hsu, Evaluation of recent intranasal drug delivery systems to the central nervous system, Pharmaceutics, 14 (2022) 629.
46. S. Talegaonkar, P. Mishra, Intranasal delivery: An approach to bypass the blood brain barrier, Indian journal of pharmacology, 36 (2004) 140–147.
47. L.M. Ensign, B.C. Tang, Y.-Y. Wang, A.T. Terence, T. Hoen, R. Cone, J. Hanes, Mucus-penetrating nanoparticles for vaginal drug delivery protect against herpes simplex virus, Science translational medicine, 4 (2012) 138ra179-138ra179.
48. H.C. Zierden, A. Josyula, R.L. Shapiro, H.T. Hsueh, J. Hanes, L.M. Ensign, Avoiding a Sticky Situation: Bypassing the Mucus Barrier for Improved Local Drug Delivery, Trends in Molecular Medicine, (2021).
49. S.K. Lai, Y.-Y. Wang, J. Hanes, Mucus-penetrating nanoparticles for drug and gene delivery to mucosal tissues, Advanced drug delivery reviews, 61 (2009) 158–171.
50. G. Osman, J. Rodriguez, S.Y. Chan, J. Chisholm, G. Duncan, N. Kim, A.L. Tatler, K.M. Shakesheff, J. Hanes, J.S. Suk, PEGylated enhanced cell penetrating peptide nanoparticles for lung gene therapy, Journal of controlled release, 285 (2018) 35–45.
51. G.A. Duncan, J. Jung, J. Hanes, J.S. Suk, The mucus barrier to inhaled gene therapy, Molecular Therapy, 24 (2016) 2043–2053.
52. L.E. Morgan, A.M. Jaramillo, S.K. Shenoy, D. Raclawska, N.A. Emezienna, V.L. Richardson, N. Hara, A.Q. Harder, J.C. NeeDell, C.E. Hennessy, Disulfide disruption reverses mucus dysfunction in allergic

airway disease, Nature communications, 12 (2021) 1–9.

53. V.Y. Lin, N. Kaza, S.E. Birket, H. Kim, L.J. Edwards, J. LaFontaine, L. Liu, M. Mazur, S.A. Byzek, J. Hanes, Excess mucus viscosity and airway dehydration impact COPD airway clearance, European Respiratory Journal, 55 (2020).
54. M. Yang, T. Yu, Y.Y. Wang, S.K. Lai, Q. Zeng, B. Miao, B.C. Tang, B.W. Simons, L.M. Ensign, G. Liu, Vaginal delivery of paclitaxel via nanoparticles with non-mucoadhesive surfaces suppresses cervical tumor growth, Advanced healthcare materials, 3 (2014) 1044–1052.
55. J. Zhou, M. Zaiss, L. Knutsson, P.Z. Sun, S.S. Ahn, S. Aime, P. Bachert, J.O. Blakeley, K. Cai, M.A. Chappell, Review and consensus recommendations on clinical APT-weighted imaging approaches at 3T: application to brain tumors, Magnetic resonance in medicine, 88 (2022) 546–574.
56. J. Zhou, B. Lal, D.A. Wilson, J. Laterra, P.C. Van Zijl, Amide proton transfer (APT) contrast for imaging of brain tumors, Magnetic Resonance in Medicine: An Official Journal of the International Society for Magnetic Resonance in Medicine, 50 (2003) 1120–1126.
57. J. Zhou, E. Tryggestad, Z. Wen, B. Lal, T. Zhou, R. Grossman, S. Wang, K. Yan, D.-X. Fu, E. Ford, Differentiation between glioma and radiation necrosis using molecular magnetic resonance imaging of endogenous proteins and peptides, Nature medicine, 17 (2011) 130–134.
58. S. Wang, E. Tryggestad, T. Zhou, M. Armour, Z. Wen, D.-X. Fu, E. Ford, P.C. van Zijl, J. Zhou, Assessment of MRI parameters as imaging biomarkers for radiation necrosis in the rat brain, International Journal of Radiation Oncology* Biology* Physics, 83 (2012) e431-e436.
59. L. Chen, Z. Wei, K.W. Chan, Y. Li, K. Suchal, S. Bi, J. Huang, X. Xu, P.C. Wong, H. Lu, D-Glucose uptake and clearance in the tauopathy Alzheimer's disease mouse brain detected by on-resonance variable delay multiple pulse MRI, Journal of Cerebral Blood Flow & Metabolism, 41 (2021) 1013–1025.
60. J. Huang, P.C. van Zijl, X. Han, C.M. Dong, G.W. Cheng, K.-H. Tse, L. Knutsson, L. Chen, J.H. Lai, E.X. Wu, Altered d-glucose in brain parenchyma and cerebrospinal fluid of early Alzheimer's disease detected by dynamic glucose-enhanced MRI, Science advances, 6 (2020) eaba3884.
61. K.W. Chan, M.T. McMahon, Y. Kato, G. Liu, J.W. Bulte, Z.M. Bhujwalla, D. Artemov, P.C. van Zijl, Natural D-glucose as a biodegradable MRI contrast agent for detecting cancer, Magnetic resonance in medicine, 68 (2012) 1764–1773.
62. S. Walker-Samuel, R. Ramasawmy, F. Torrealdea, M. Rega, V. Rajkumar, S.P. Johnson, S. Richardson, M. Gonçalves, H.G. Parkes, E. Årstad, In vivo imaging of glucose uptake and metabolism in tumors, Nature medicine, 19 (2013) 1067–1072.
63. J. Huang, J.H. Lai, X. Han, Z. Chen, P. Xiao, Y. Liu, L. Chen, J. Xu, K.W. Chan, Sensitivity schemes for dynamic glucose-enhanced magnetic resonance imaging to detect glucose uptake and clearance in mouse brain at 3 T, NMR in Biomedicine, (2021) DOI: 10.1002/nbm.4640.
64. K. Ward, A. Aletras, R.S. Balaban, A new class of contrast agents for MRI based on proton chemical exchange dependent saturation transfer (CEST), Journal of magnetic resonance, 143 (2000) 79–87.
65. L. Toschi, G. Finocchiaro, S. Bartolini, V. Gioia, F. Cappuzzo, Role of gemcitabine in cancer therapy, Future oncology, 1 (2005) 7–17.

66. S. Mirzaei, M. Khalilian, A.A. Taherpour, Mechanistic study of the hydrolytic degradation and protonation of temozolomide, RSC Advances, 5 (2015) 41112–41119.
67. L. de Sousa Cavalcante, G. Monteiro, Gemcitabine: metabolism and molecular mechanisms of action, sensitivity and chemoresistance in pancreatic cancer, European journal of pharmacology, 741 (2014) 8–16.
68. A.J. van Hell, A. Haimovitz-Friedman, Z. Fuks, W.D. Tap, R. Kolesnick, Gemcitabine kills proliferating endothelial cells exclusively via acid sphingomyelinase activation, Cellular signalling, 34 (2017) 86–91.
69. K.W. Chan, T. Yu, Y. Qiao, Q. Liu, M. Yang, H. Patel, G. Liu, K.W. Kinzler, B. Vogelstein, J.W. Bulte, A diaCEST MRI approach for monitoring liposomal accumulation in tumors, Journal of controlled release, 180 (2014) 51–59.

Figures

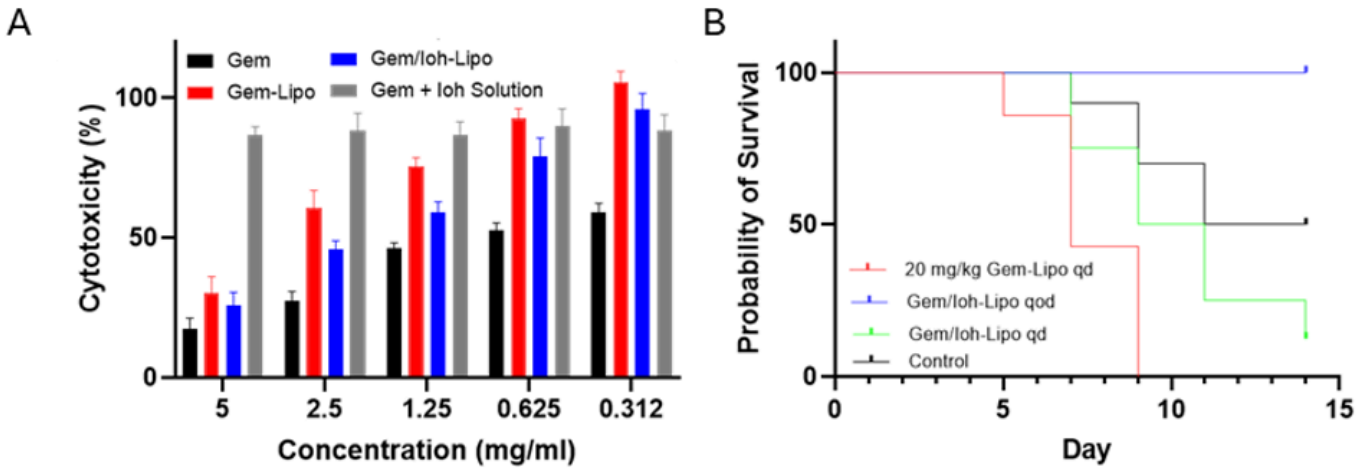


Figure 1

Optimization of the treatment formulation. In-vitro cytotoxicity and In-vivo survival Assessment. (A) In vitro cytotoxicity MTT assay. Cells were incubated with gemcitabine solution, Gem-Lipo, Gem/Ioh-Lipo, and Gemcitabine iohexol coloaded liposome (0.312 mg/mL to 5 mg/mL) 72 hours to evaluate cytotoxicity by MTT assay. (B) Kaplan-Meier curves for 4 groups of treatment regimen (a) 20 mg/kg Gem-Lipo daily treated group, (b) 10 mg/kg Gem-Lipo alternative day treated group, (c) 10 mg/kg Gem-Lipo daily treated group (d) control group.

A

Liposome	Concentration (particles/ml)	Size (nm)	PDI	Zeta Potential (mV)
Ioh-Lipo	$6.23\pm1.35\times10^{16}$	166.3±0.7	0.20±0.02	-5.8±0.07
Gem-Lipo	$7.55\pm1.04\times10^{16}$	144.9±1.0	0.19±0.02	-5.3±0.04
Ioh/Gem-Lipo	$6.94\pm0.17\times10^{16}$	153.9±0.4	0.20±0.01	-5.0±0.10
Blank-Lipo	$9.27\pm2.46\times10^{16}$	142.8±0.4	0.1±0.01	-4.8±0.03

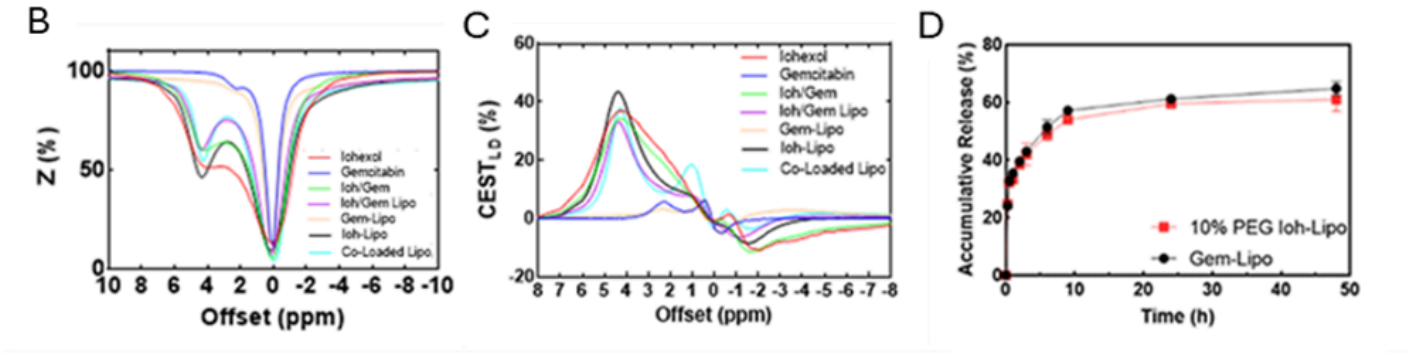


Figure 2

Liposome characterization and CEST properties of iohexol, gemcitabine, blank-Lipo, Gem/Ioh-Lipo, Ioh-Lipo, Gem-Lipo and Co-Loaded Lipo (n=3). (A) Table of liposome characterization of Ioh-Lipo, Gem-Lipo, Ioh/Gem-Lipo, blank-Lipo and (B) Z spectra, (C) $CEST_{LD}$ under1.0 μT and pH 7.0. d Release profiles of Ioh-Lipo and Gem-Lipo

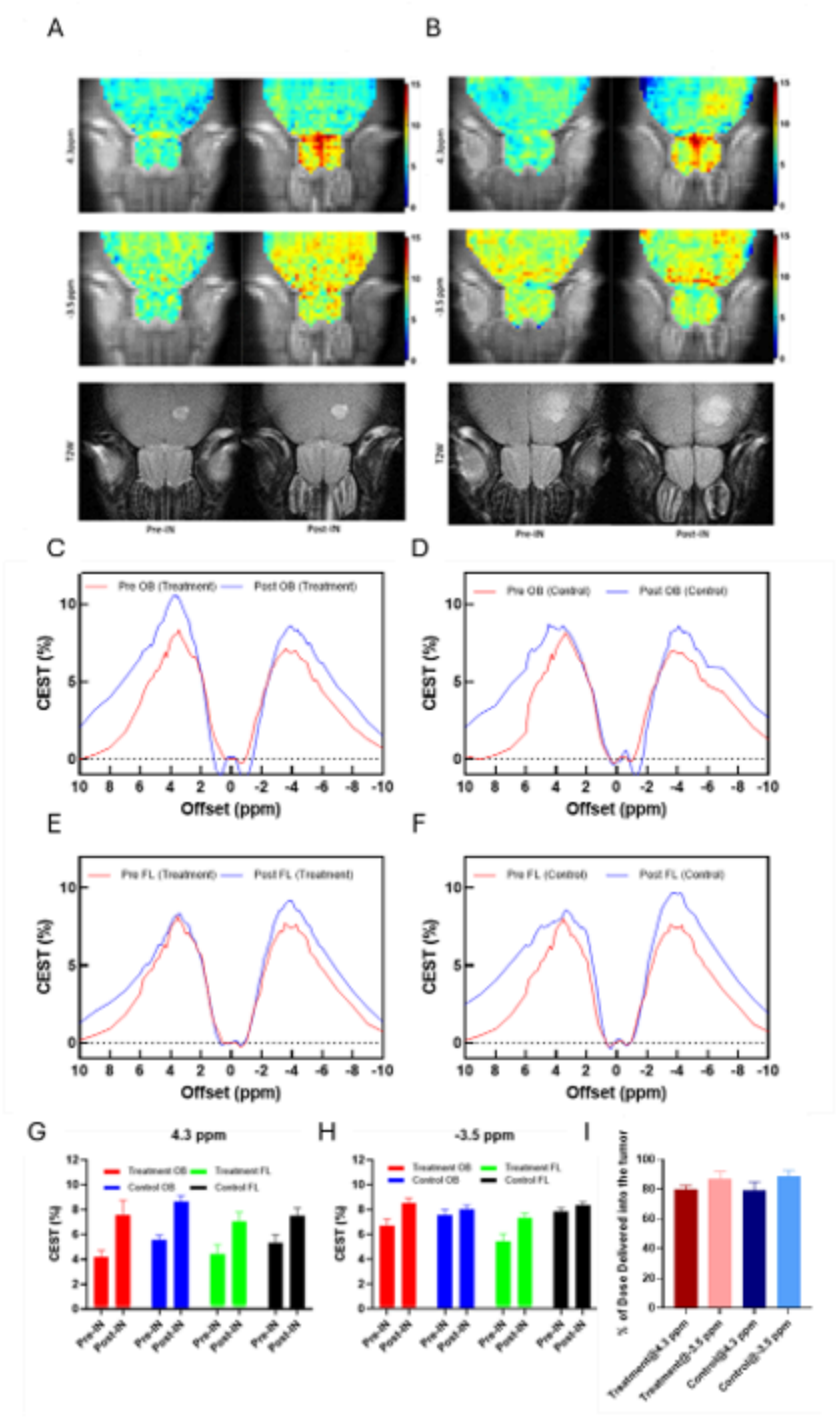


Figure 3

Representative MR images for the in vivo liposomal distribution of pre-IN and post-IN of treatment group and control group. (A) Pre-IN and post-IN CEST map at 4.3 ppm and -3.5 ppm of treatment group, (B) Pre-IN and post-IN CEST map at 4.3 ppm and -3.5 ppm of control group, (C) CEST spectrum of treatment group in OB, (D) CEST spectrum of control group in OB, (E) CEST spectrum of treatment group in FL, (F) CEST spectrum of control group in FL, (G) CEST comparison (n=5) in OB and FL of pre-IN and post-IN of treatment group and control group at 4.3 ppm, (H) at -3.5 ppm, and (I) relatively high percentage dose of

liposome delivered into the tumor from OB of treatment group and control group at 4.3 ppm and -3.5 ppm, with comparable dose delivered.

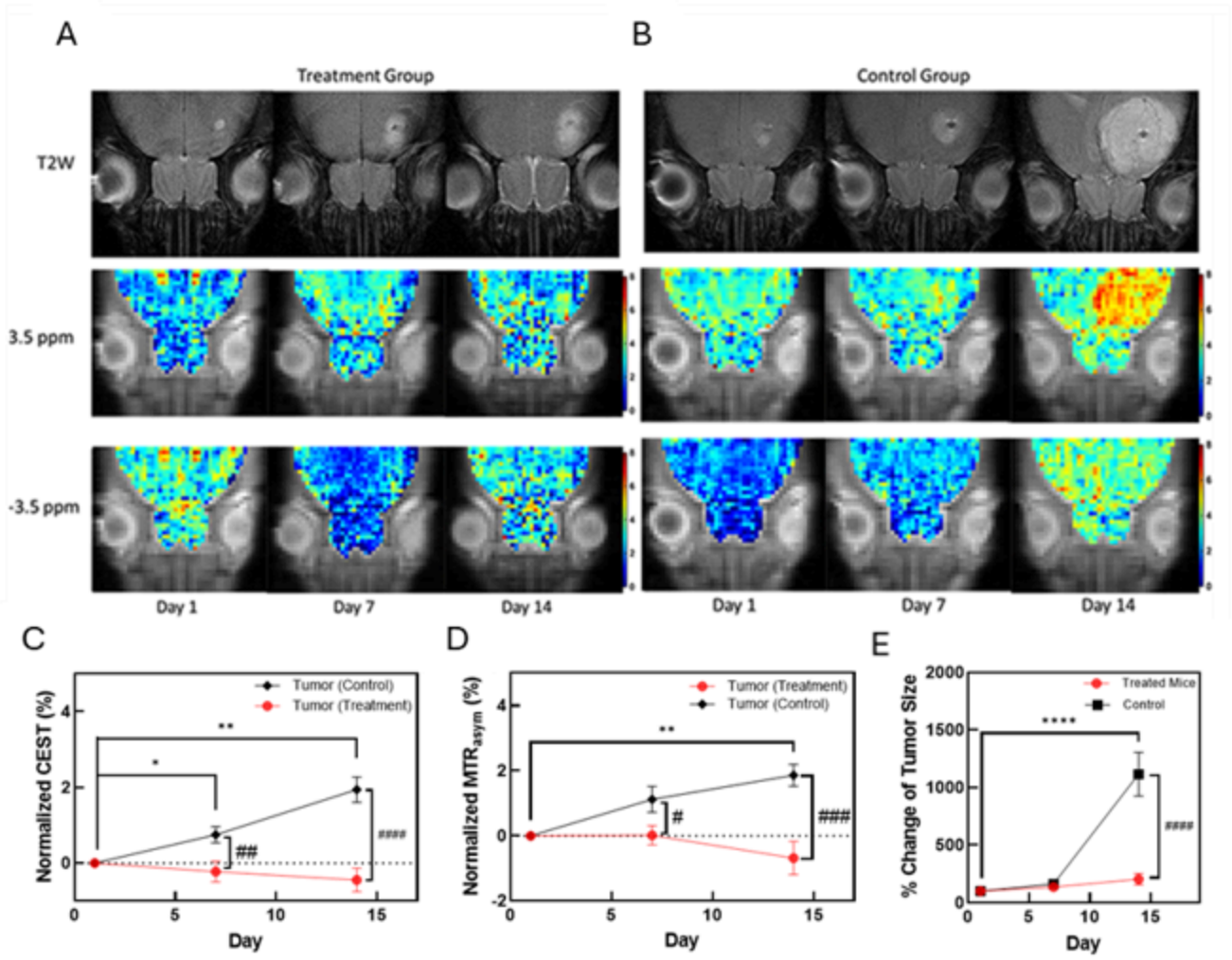


Figure 4

Representative MR images for the treatment group and control group and quantification of tumor monitoring of treatment group and control group (n=5). **a** T2w image, CEST map at 3.5 ppm, and -3.5 ppm of treatment group **b** T2w image, CEST map at 3.5 ppm, and -3.5 ppm of control group. **c** Normalized CEST contrast change at 3.5ppm, **d** Normalized MTR_{asym} change from Day 1, Day7, and Day 14 in the tumor region. **e** Percentage change of tumor size of (red) treatment group and (black) control group (n=5). Comparisons were made between the groups using two-way ANOVA and multiple t-test. Differences were considered as statistically significant for P value < 0.05 (*/#), P < 0.01 (**/##), and P<0.001 (***/###), and P<0.0001 (****).

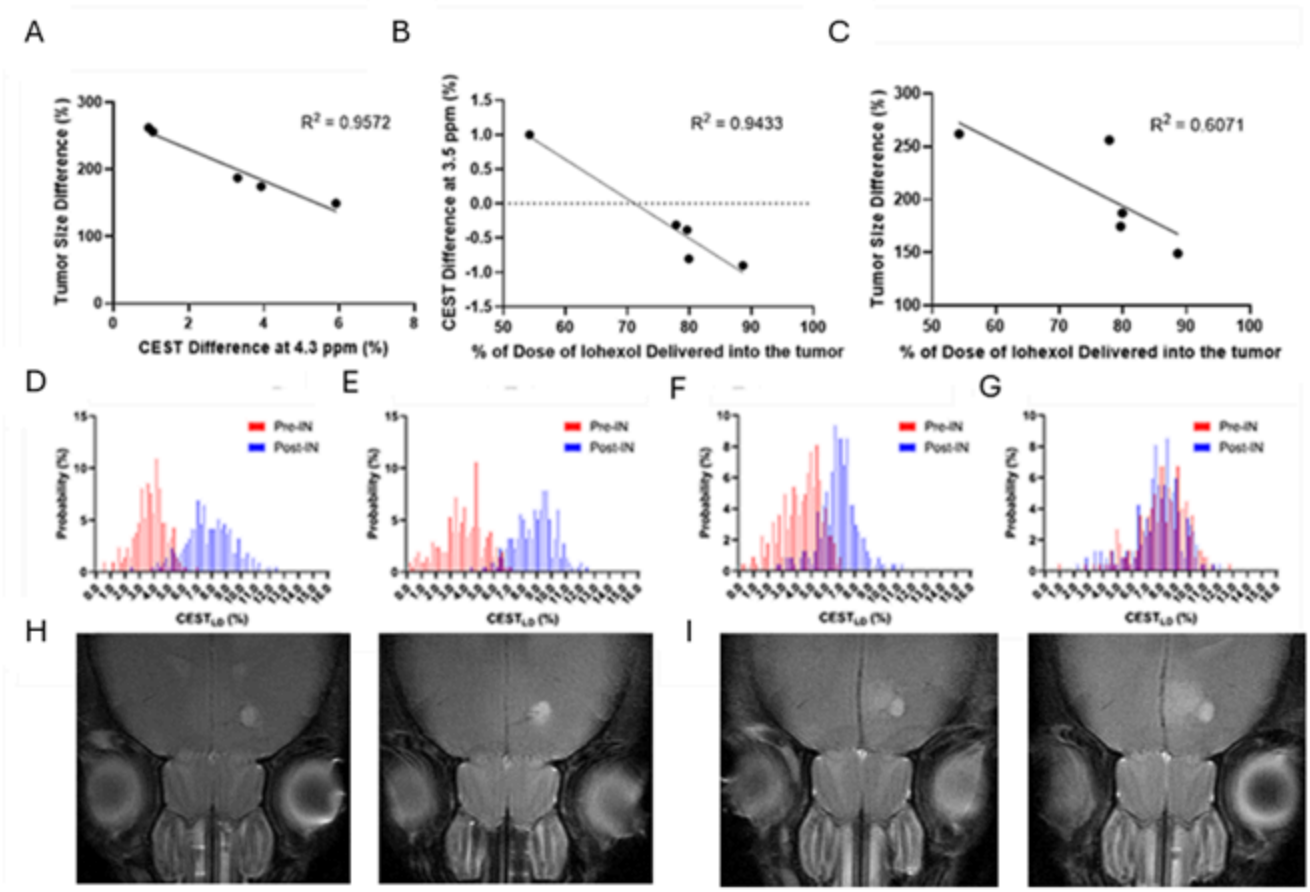


Figure 5

Quantitative correlation of efficacy of intranasal drug delivery with anatomical and molecular therapeutic outcomes. (A) Linear regression analysis correlating the anatomical therapeutic response (tumor size difference, %) with the CEST signal in the OB at 4.3 ppm (tracking drug content). (B) Correlation between early molecular therapeutic efficacy, evaluated via APTw signal change (CEST difference at 3.5 ppm), and the percentage dose of iohexol delivered into the tumor. (C) Correlation between the resulting anatomical therapeutic response (tumor size difference, %) and the percentage dose of iohexol delivered into the tumor. (D-G) Representative histograms depicting the pixel-wise CEST signal distribution in the OB Pre-IN and Post-IN. Data are shown for a representative subject exhibiting a high therapeutic effect at d 4.3 ppm and e -3.5 ppm, contrasted with a subject exhibiting a low therapeutic effect at f 4.3 ppm and g -3.5 ppm. (H, I) Representative T_2-weighted MR images utilized for longitudinal tumor size quantification (Day 1 and Day 7) in the h high-effect and i low-effect treatment groups. Data points represent individual subjects. Solid lines denote linear regression fits, with corresponding R^2 values indicated for each plot.

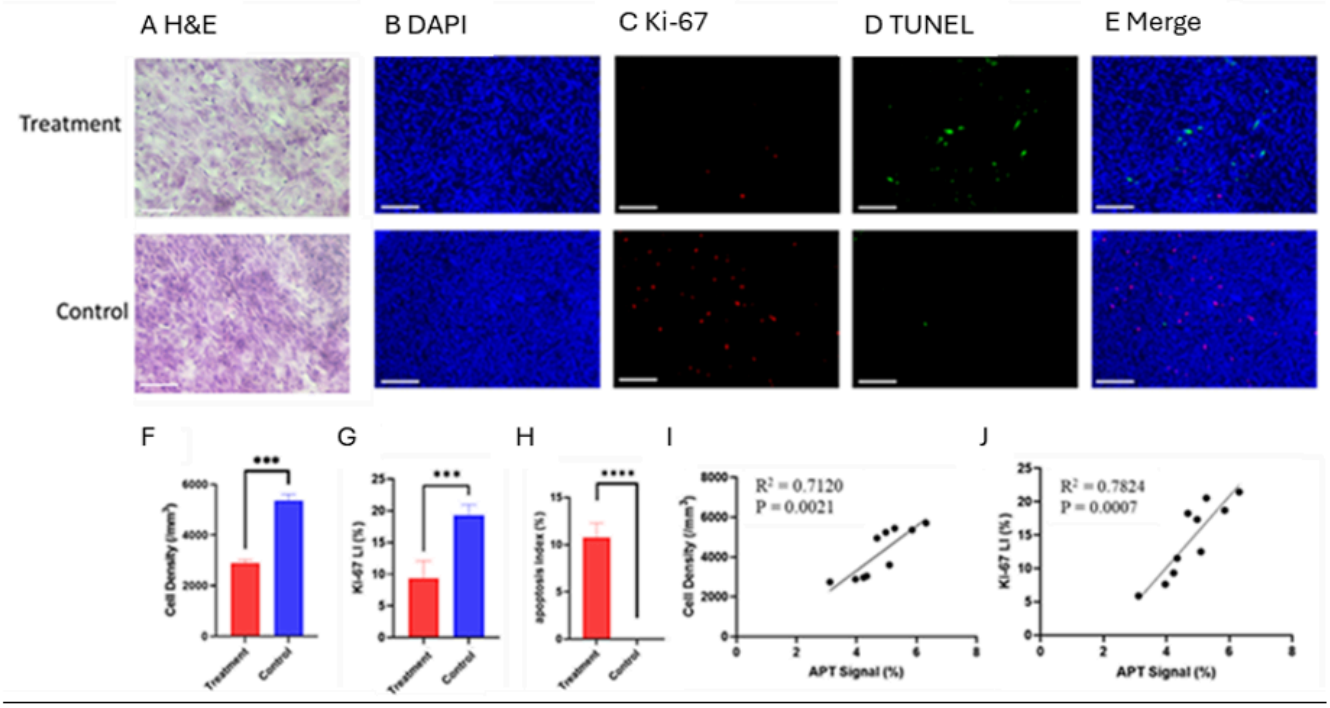


Figure 6

Histology and its evaluation of the GBM in the mouse brain with the treatment and control group on day 14. (A) Representative H&E staining of the mouse brain slice for two groupsThe fluorescence images of (B) DAPI, (C) Ki-67, (D) Tunel and (E) Merge (Scale bar = 200 μm). (F) Cell density, (G) Ki-67 labeling index and (H) Apoptosis index between two groups (n = 5 per group). Correlations between APT signal with (I) cell density and (J) Ki-67 labeling index (n = 10). Data were presented as mean ± SD (*** $p < 0.001$, **** $p < 0.0001$, Two-tailed t-test).

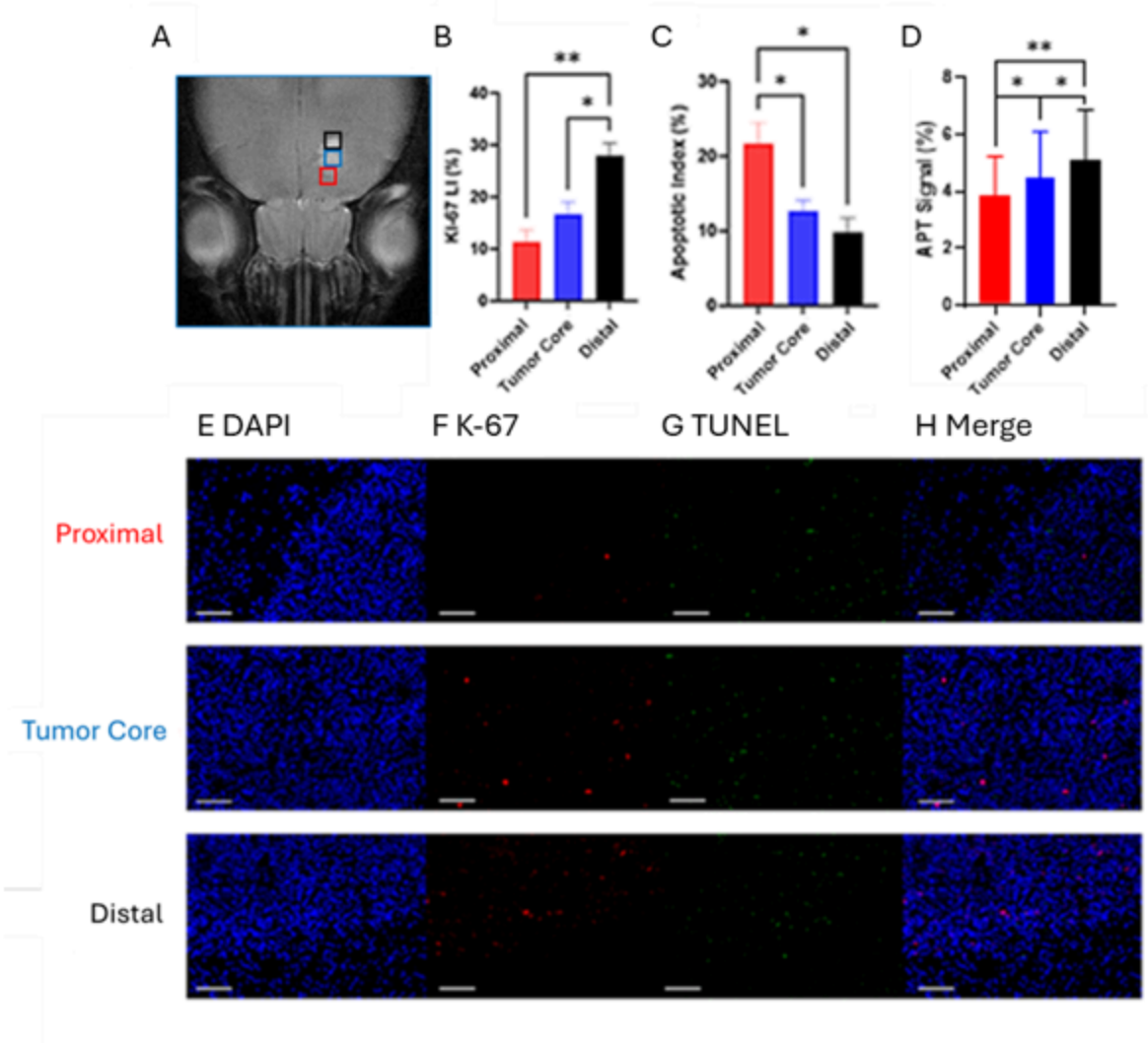


Figure 7

The histopathologic spatial analysis of tumor in the treatment group on day 14 (n = 5 per group). (A) Representative T1w image of treatment group with 3 regions for quantitative regional analysis of (B) Ki-67 LI, (C) apoptotic index, (D) APT signal of three subregions. The fluorescence images of (C) DAPI, (D) Ki-67, (E) TUNEL, (F) Merge with three regions (Top: Proximal region, middle: Tumor Core region, Bottom: Distal Region. (Scale bar = 200 μm) Data were presented as mean ± SEM (* $p < 0.05$, ** $p < 0.01$, Two-Way ANOVA)

Supplementary Files

This is a list of supplementary files associated with this preprint. Click to download.

- SupplementaryInformation.docx